Volume 2
Number 5
September 2025
Pages 841-1190

RSC Pharmaceutics

rsc.li/RSCPharma

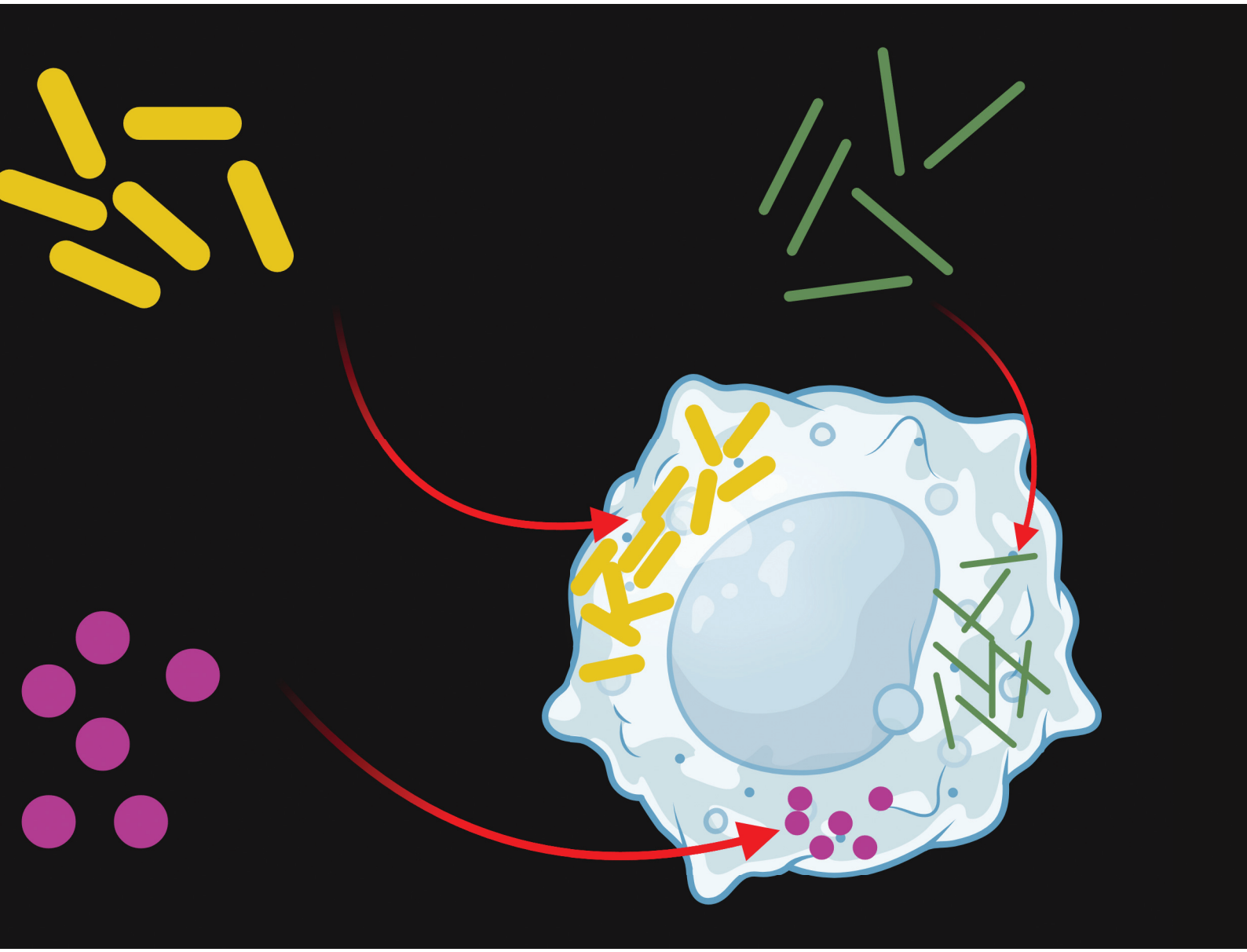

eISSN 2976-8713

ROYAL SOCIETY OF CHEMISTRY

PAPER

Padma V. Devarajan *et al.*

Effect of shape on cellular internalization and anti-cancer efficacy of hydroxyapatite nanoparticles in an osteosarcoma cell line

RSC Pharmaceutics

ROYAL SOCIETY OF CHEMISTRY

PAPER

View Article Online
View Journal | View Issue

Check for updates

Cite this: *RSC Pharm.*, 2025, **2**, 1087

Effect of shape on cellular internalization and anti-cancer efficacy of hydroxyapatite nanoparticles in an osteosarcoma cell line†

Simmi Gupta,‡ Esha S. Attar,‡ Vishvesh Joshi§ and Padma V. Devarajan *

Received 10th January 2025,
Accepted 1st March 2025

DOI: 10.1039/d5pm00005j

rsc.li/RSCPharma

Hydroxyapatite nanoparticles (HAP NPs) with distinct morphologies were synthesized by the wet precipitation method by varying pH, and their shape was confirmed by scanning electron microscopy as spherical (pH 12), rod-like (pH 9), and needle-like (pH 8). The particle sizes of HAP NPs were 96.86 ± 1.48 nm for needle-shaped, 118 ± 4.32 nm for rod-shaped, and 94.43 ± 1.02 nm for spherical-shaped particles. XRD analysis showed clear and distinct peaks indicating crystalline nature, while FTIR confirmed the characteristic features of hydroxyapatite. The negative zeta potential of the HAP NPs was attributed to the presence of surface phosphate ions. The influence of HAP NP shape and size on intracellular uptake was evaluated in the MG-63 osteosarcoma cell line by Confocal Laser Scanning Microscopy (CLSM). CLSM results demonstrated that rod-shaped HAP NPs predominantly localized within the lysosome and nucleus, while spherical HAP NPs accumulated at the cell membrane. The MTT, clonogenic survival, cell scratch and transwell migration assays revealed that rod-shaped HAP NPs exhibited superior anticancer activity compared to their needle- and spherical-shaped counterparts and completely suppressed the clonogenic survival of MG-63 cells. Our findings confirm that the shape of HAP NPs is a critical factor influencing their intracellular uptake and anticancer activity.

Introduction

Hydroxyapatite is the principal inorganic building block of bones.[1–4] It is suggested that nanosized hydroxyapatite (HAP) particles self-assemble and provide mechanical strength and flexible structures to bones.[5–8] Interestingly, HAP NPs have also been reported to inhibit the proliferation of various cancer cell lines including melanoma,[9] colon,[10] breast,[11] gastric,[12] hepatoma,[13,14] glioma[15] and human cervical adenocarcinoma[16] and can inhibit proliferation and trigger apoptosis in osteosarcoma cell lines. The anticancer activity of HAP NPs is elicited through mechanisms such as disrupting mitochondrial function, arresting the cell cycle and/or altering intracellular signaling pathways essential for cell survival.

HAP NP uptake by cancer cells is influenced by physicochemical properties like morphology, crystal size and surface charge. For instance, when the crystallinity of HAP NPs decreases, the increased solubility in body fluids can negatively impact their interaction with cells. Similarly, the shape and structure of HAP NPs can influence cell behaviour by altering the surface area available for cell contact.[17–21] HAP NPs exhibit concentration-dependent growth inhibition of osteosarcoma cells, with higher concentrations of HAP NPs resulting in augmented reduction in cell viability and apoptosis induction. HAP NPs also interact with the extracellular matrix, amplifying their cytotoxic effects on cancer. Liu *et al.* explored the use of nano-hydroxyapatite (HAP NPs) as a targeted delivery vehicle for doxorubicin, to treat bone cancers.[18,22–25] Studies revealed that the anticancer effect was aided by their direct interaction with cells, which facilitated internalization of the HAP nanoparticles (HAP-NPs).[26–33] Furthermore, Han *et al.* discovered that nanosized HAP was more toxic to cancer cells than micron-sized HAP due to the higher internalization of HAP NPs in cancer cells.[34]

Nanoparticle shape can be a key determinant influencing internalization pathways and cellular uptake efficiency. For cancer treatment, tailoring the shape of HAP NPs can potentially enhance their internalization in cancer cells, enhance localized drug concentration and thereby improve therapeutic outcomes.[35,36] The effect of nanoparticle size on cell internalization and anticancer efficacy is demonstrated;[37,38] however, studies on the effect of HAP NP shape on cell uptake and anticancer efficacy are limited. One study demonstrated a favored

Department of Pharmaceutical Sciences and Technology, Institute of Chemical Technology Matunga (E), Mumbai-400019, India. E-mail: pvdevarajan@gmail.com; Fax: +9122 33611020; Tel: +91 22 3361 2201

†Electronic supplementary information (ESI) available. See DOI: https://doi.org/10.1039/d5pm00005j

‡Equal contribution.

§Currently at Chartwell Pharmaceuticals LLC, 77 Brenner Dr, Congers, NY 10920.

uptake of rod-like HAP nanoparticles[39] and attributed the same to enhanced interaction through van der Waals forces due to their larger surface area.[36]

In this study, our premise was that the naturally high affinity of HAP for bone could localize the HAP NPs in bone, while their anticancer activity could be tailored for maximal efficacy by modifying the NP shape. The objectives of the present study therefore included evaluation of the effect of the shape of HAP NPs on intracellular uptake and anticancer efficacy in the MG-63 osteosarcoma cell line, as well as *ex vivo* assessment of the affinity of HAP NPs for bone.

Materials and methods

Materials

Calcium dinitrate tetrahydrate, di-ammonium hydrogen orthophosphate, cetyltrimethyl ammonium bromide (CTAB), and sodium hydroxide (NaOH) were procured from SD Fine Chem Limited (SDFCL, India). Coumarin 6 was bought from Sigma-Aldrich (USA). Other chemicals were obtained from Invitrogen (USA), including CellMask, DAPI, LysoTracker, and Neutral Red. Additional reagents were sourced from Himedia (Mumbai, India), including Dulbecco's modified Eagle medium (DMEM), penicillin/streptomycin, fetal bovine serum (FBS), MTT, T-25 and T-75 flasks, and 12-, 24-, and 96-well plates, and Corning Life Sciences, Bedford, MA, supplied 24-well plate control inserts (8.0 microns). The human osteosarcoma cell line (MG-63) was acquired from NCCS, Pune, India. The rest of the chemicals and solvents utilized were of analytical quality.

Preparation of HAP NPs

The wet chemical precipitation method described earlier[40] was used to prepare rod-shaped, needle-shaped and spherical HAP NPs. A 10 ml aqueous solution of 0.06 M diammonium hydrogen phosphate was added dropwise to a 10 ml aqueous solution of calcium nitrate tetrahydrate (0.1 M) containing CTAB (10 mg) under magnetic stirring, with the pH maintained at 8, 9, and 12 using 1 N NaOH to obtain the rod-shaped, needle-shaped and spherical HAP NPs, respectively. The NP dispersion was centrifuged at 10 000 rpm and washed until the supernatant attained a pH of 7–7.4. The pellets were sonicated in 10 mL of distilled water for 5 minutes. The dispersion was freeze-dried utilizing a Labconco freeze dryer to obtain HAP nanoparticles. The freeze-drying process lasted for 12 hours under a vacuum ranging from 10 to 50×10^{-3} bar, while ensuring that the surface temperature of the condenser remained below −50 °C. Particle size was monitored before and after freeze-drying, and the size after freeze-drying (Sf) was compared with the initial size (Si), and Sf/Si was calculated.

Fluorescent dye-labelled HAP NPs

Green fluorescent dye Coumarin 6-labelled HAP NPs were prepared to visualize the cellular internalization of NPs. HAP NPs of the three different shapes were incubated in an alcoholic solution of Coumarin 6 in ethanol (1 mg mL^{-1}) for 15 min at 27 °C. The surplus dye was removed by centrifugation at 5000 rpm for 10 min.

Characterization of HAP NPs

Particle size distribution and zeta potential. Particle size, zeta potential and electrophoretic mobility were evaluated by Dynamic Light Scattering (DLS), Phase Analysis Light Scattering (PALS) and Electrophoretic Light Scattering (ELS), respectively, on a Brookhaven instrument.

Scanning electron microscope (SEM) analysis. The shape of SCT HAP nanoparticles was determined by scanning electron microscopy (SEM). First, the nanoparticles were dispersed in filtered double-distilled water, and a small drop of this dispersion was carefully placed on a piece of carbon tape, which served as a conductive and stable support for SEM imaging. Next, a thin layer of gold–palladium was applied using a process called sputter coating. The prepared sample was imaged on a JEOL JSM-6510 SEM (Tokyo, Japan).

XRD analysis. X-ray diffraction spectra of the HAP nanoparticles were recorded using an X-ray diffractometer (XRD, D/MaxIIIA, RIGAKU, Japan), with Cu-Kα X-rays of a wavelength (λ) of 1.5406 Å. Measurements were taken within the 2θ range of 10° to 80° with an increment of 0.02°.

FTIR analysis. FT-IR spectroscopy was carried out on a thin, transparent pellet formed by mulling a sample of HAP NPs, with KBr, and compressing it into a thin disc, using a Perkin Elmer RX1 spectrometer.

Cell culture. MG-63 cells, originating from human osteosarcoma, were grown in Dulbecco's modified Eagle medium (DMEM) supplemented with 10% fetal bovine serum (FBS) and a mixture of antibiotics consisting of 1000 IU of penicillin and 10 mg mL^{-1} streptomycin. The cells were maintained at 37 ± 2 °C in a humidified environment with 5% CO_2.

Intracellular uptake by confocal laser scanning microscopy (CLSM). The MG-63 cells were transferred into wells of a 24-well plate at 50 000 cells per mL and cultured for 24 hours at 37 ± 2 °C in a humidified atmosphere containing 5% CO_2. Subsequently, the cells were exposed to the rod-shaped, needle-shaped and spherical coumarin-labelled HAP NPs (cHAP NPs) at a concentration of 100 μg mL^{-1} and allowed to stand for 2 hours. Following the incubation period, the cells were washed thrice using PBS to eliminate the uninternalized cHAP NPs. The cells were fixed using a 4% w/v paraformaldehyde solution for 10 minutes at ambient temperature, rinsed twice with phosphate buffer and incubated at 37 ± 2 °C for 30 minutes. The cells were then stained with 75 μM LysoTracker (lysosomal marker) and 0.1 μM CellMask (plasma membrane marker) for 10 minutes and then subjected to two PBS washes. DAPI, a nuclear stain, was added to each well at a dilution of 1 : 10 000 and incubated for 10 minutes at 37 °C. Multichannel confocal microscopy was performed using a Leica microscope, with excitation wavelengths for coumarin-labeled HAP NPs, LysoTracker, CellMask, and DAPI at 457, 577, 633, and 405 nm, respectively.

In vitro anticancer efficacy

MTT assay. MG-63 cells were seeded at a concentration of 10 000 cells per mL in a culture plate with 96 wells, which contained DMEM. The plates were placed in a humidified atmosphere containing 5% CO_2 and maintained at a temperature of 37 ± 2 °C for the duration of the incubation. The cells were then treated with the rod-shaped, needle-shaped, and spherical HAP NPs at three different concentrations of 150, 250, and 500 μg mL^{-1} for 72 hours. Untreated cells served as the control. Following treatment, 10 μL of a 5 mg mL^{-1} MTT solution was introduced into each well, and the plates were incubated at 37 ± 2 °C for 2 hours to promote the formation of formazan crystals. The liquid was gently aspirated, followed by addition of 100 μL DMSO to dissolve the formazan crystals. The absorbance at 570 nm was measured using a plate reader. The IC_{50} values for the HAP NPs of different morphologies were determined from the percent inhibition and concentration data.

Clonogenic assay. The MG-63 cells were added to a plate containing 6 wells at a concentration of 1000 cells per mL and left to bind overnight. The cells were exposed to the HAP NPs of rod, needle, and spherical shapes at concentrations of 250 and 500 μg mL^{-1}, allowed to stand for 8–10 days, and observed for colony formation. The colonies were immobilized with methanol, stained with crystal violet, and observed using an inverted microscope. The survival fraction (SF) and plating efficiency (PE) were calculated using the following formulae:[27]

$$\text{SF} = \text{number of colonies} \times 100/\text{number of cells plated} \times \text{plating efficiency},$$

and

$$\text{PE} = \text{number of colonies in the control sample}/\text{number of cells plated}$$

Plots of survival fraction *vs.* concentration were constructed.

Cell scratch assay. MG-63 cells were seeded at a concentration of 20 000 cells per mL in 12-well plates and allowed to proliferate for 72 hours at 37 ± 2 °C in a moist environment containing 5% CO_2. Upon reaching full confluence, a linear scratch was made on the cell monolayer using a sterile 200 μL pipette tip and the cell remnants were removed to obtain a distinctly visible scratch line. The cells were treated with rod-shaped, needle-shaped and spherical HAP NPs at a concentration of 100 μg ml^{-1}. The plates were monitored under an inverted microscope for up to 48 hours for closure of the scratch.[41]

Transwell migration assay. The upper donor chambers of a 24-well transwell insert (8.0 micron pore size) were seeded with MG-63 cells at a density of 20 000 cells per mL. The cells were allowed to proliferate at 37 ± 2 °C in a humid atmosphere with 5% CO_2 for 48 hours. HAP NPs (100 μg mL^{-1}) of rod, needle and spherical shapes were carefully added on top of the cells, in the upper chamber. Complete DMEM (600 μL) was added to the lower receptor chambers. The transwells were then incubated for 24 hours at 37 ± 2 °C in a moist atmosphere with 5% CO_2. At the end of 24 hours, the cells that had migrated into the receptor chambers through the membrane were fixed using 70% ethanol for 10 minutes. The cells were then treated with crystal violet and visualized under a microscope, and the count of cells in several fields of view was recorded.

Hoechst/PI double staining assay. The MG-63 cells were seeded in a plate having 24 wells, at a concentration of 1.0 million cells per mL and permitted to proliferate for 24 hours at 37 ± 2 °C in a moist environment with 5% CO_2. Coumarin-labelled HAP NPs (500 μL) of the three different shapes at a concentration of 100 μg mL^{-1} were introduced into the wells and the plates were incubated at 37 ± 2 °C in a humid environment with 5% CO_2. Following a PBS wash, the cells were subjected to staining with the dyes Hoechst 33258 (5 μg mL^{-1}) and propidium iodide (10 μg mL^{-1}), both of which were prepared in complete DMEM. The cells were allowed to stand in the dark at a temperature of 37 ± 2 °C for 15 minutes. The medium was aspirated and the cells were rinsed with phosphate buffer and then examined under a multichannel confocal (Leica) microscope.

Statistical analysis. The data are stated as the mean ± standard deviation of at least three independent experiments. Data were analysed using one-way ANOVA with a *post hoc* test on GraphPad Prism 8.0, wherein $p < 0.05$ was considered as statistically significant.

Results and discussion

Hydroxyapatite nanoparticles synthesized by the wet precipitation method at pH 8, 9, and 12 resulted in needle-shaped, rod-shaped and spherical HAP NPs, respectively. Fluorescent coumarin-labeled HAP NPs were obtained by incubating the NPs in coumarin solution. Coumarin 6 was effectively loaded onto the NPs irrespective of their shape.

Characterization of HAP NPs

The SEM photomicrographs (Fig. 1) revealed HAP NPs with smooth surface morphology, which were needle-shaped, rod-shaped, and spherical at pH 8, 9 and 12 respectively. These data corroborated earlier reports on pH and HAP NP shape.[42,43] The concentration of hydroxide (OH^-) ions played a significant role in the growth as well as the shape of the nanoparticles. A high concentration of OH^- ions (pH 12) resulted in greater adsorption of OH^- onto the complete surface of the HAP nucleus, thereby promoting unconfined isotropic and multi-dimensional growth, resulting in spherical HAP NPs. Conversely, at a medium concentration of OH^- ions (pH 9), a minimal quantity of OH^- is anticipated to be released and adsorbed at specific locations on the HAP nucleus, leading to weak, isotropic growth resulting in nano-rods. Such a decrease in OH^- concentration was advantageous for the confined and directional growth of HAP nanoparticles. However, further lowering the pH (pH 8) restricted the adsorption of OH^- ions onto the HAP nuclei, resulting in anisotropic growth and crys-

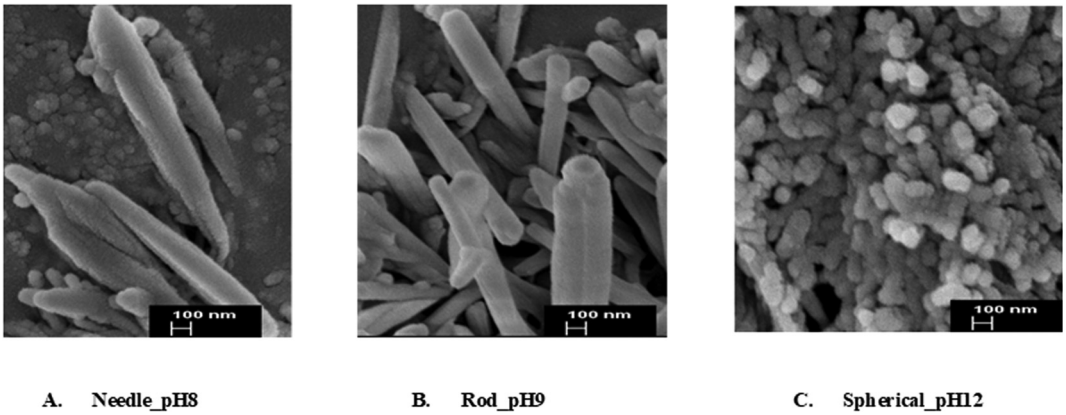

Fig. 1 Scanning electron microscopy (SEM) images of hydroxyapatite nanoparticles (HAP NPs): (A) Needle_pH 8, (B) Rod_pH 9, and (C) Spherical_pH 12 (n = 3, mean ± SE).

tallization, which favoured the formation of needle-shaped particles.[44]

The size of the needle-shaped HAP NPs was 96.86 ± 1.48 nm (PDI – 0.148 ± 0.04), rod-shaped HAP NPs was 118 ± 4.32 nm (PDI – 0.168 ± 0.08) and spherical HAP NPs was 94.43 ± 1.02 nm with a PDI of 0.144 ± 0.02. Fig. S1A† represents the multimodal size distribution curve of the spherical HAP NP dispersion. A maximum dimension of ~100 nm of the HAP NPs could provide the dual advantage of prolonged circulation and the ability to traverse into the bone trabecular architecture.

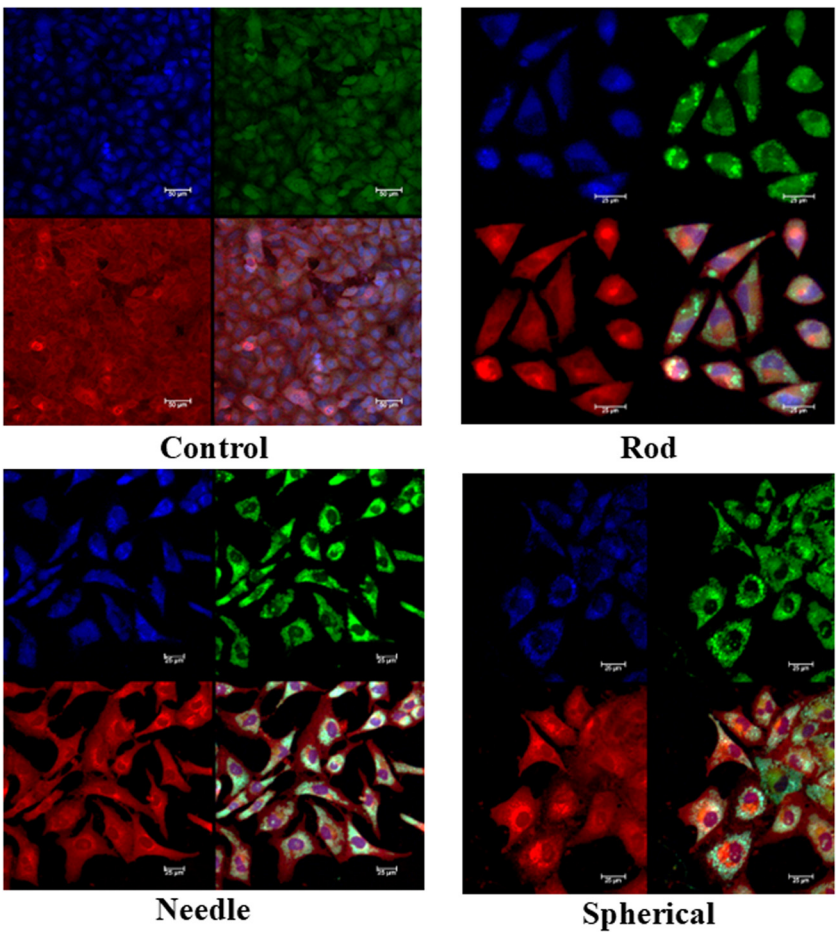

Fig. 2 Confocal laser scanning microscopy: green fluorescent rod-shaped HAP NP uptake by MG-63 osteosarcoma cells. DAPI (blue) and LysoTracker (red). The internalized rod-shaped HAP NPs inside the MG-63 cells are localized at the lysosome and nucleus. Scale bar = 50 μm (n = 3, mean ± SE).

The Phase Analysis Light Scattering (PALS) for surface charge evaluation of nanoparticles and other nanomaterials determines the zeta potential of colloidal suspension. Zeta potential is the electric charge located a short distance from the particle's surface. The negative zeta potential values of −15.50, −20.38, and −39.17 mV for the needle-shaped, rod-shaped and spherical HAP NPs, respectively, are attributed to the presence of phosphate ions on the surface of the NPs. Fig. S1B† represents the PALS report for spherical HAP NPs. The zeta potential values also suggest the stability of the HAP NP dispersions.

Another component of nanoparticle physicochemical characterization is electrophoretic mobility, which can be determined by Electrophoretic Light Scattering (ELS). ELS measures the movement of particles through a fluid under an electric field, expressed as electrophoretic mobility (μ_E). This movement is driven by the charges present on the particle's surface. The μ_E values of the spherical, rod-shaped and needle-shaped HAP NPs were −3.60, −1.60, and −1.21 (μ s^{-1})/(V cm^{-1}), respectively. Fig. S1C† shows the ELS data for spherical HAP NPs.

XRD analysis revealed diffractograms with a clear baseline and well-defined peaks. The diffraction pattern of HAP-NPs shown in Fig. S2† exhibited peaks in the range of 10–90° 2θ values: (i) 43.89°, 64.25° and 77.35° for spherical-shaped HAP NPs, (ii) 43.89°, 64.25° and 77.36° for rod-shaped HAP NPs and (iii) 31.62°, 32.44° and 77.35° for needle-shaped HAP NPs, indicating the crystalline nature of the HAP NPs. The analysis using X-ray diffraction revealed that the HAP nanoparticles consisted of highly crystalline and single-phase HAP, with no detectable impurity phase. The configuration of the diffraction peaks indicated that the sample may be thoroughly crystallized. The widened appearance of these diffraction peaks suggests that the sample dimensions are at the nanometer scale.[40]

Fourier Transform Infrared Spectroscopy (FTIR) is commonly used to analyze hydroxyapatite (HAP), particularly for identifying its characteristic functional groups and assessing its purity, crystallinity, and structural properties. In this study, FTIR analysis confirmed the presence of hydroxyapatite with its characteristic features. The characteristic overlay bands are shown in Fig. S3.† Two bands observed at 2920 cm^{-1} and 599 cm^{-1} are attributed to the stretching mode and librational mode of hydrogen-bonded OH^- ions, respectively, which are crucial components of the hydroxyapatite crystal structure. The band at 1020 cm^{-1} arises from the v3 asymmetric stretching mode of the PO_4^{3-} bond, one of the most prominent regions in the HAP spectra. The bands at 833 cm^{-1} and 559 cm^{-1} arise from the v4 bending mode of the PO_4^{3-} bond.

Intracellular uptake using confocal laser scanning microscopy (CLSM). Cellular uptake is critical to ensure the efficacy of NPs. Representative images of coumarin labelled HAP NPs are depicted in Fig. S4.†

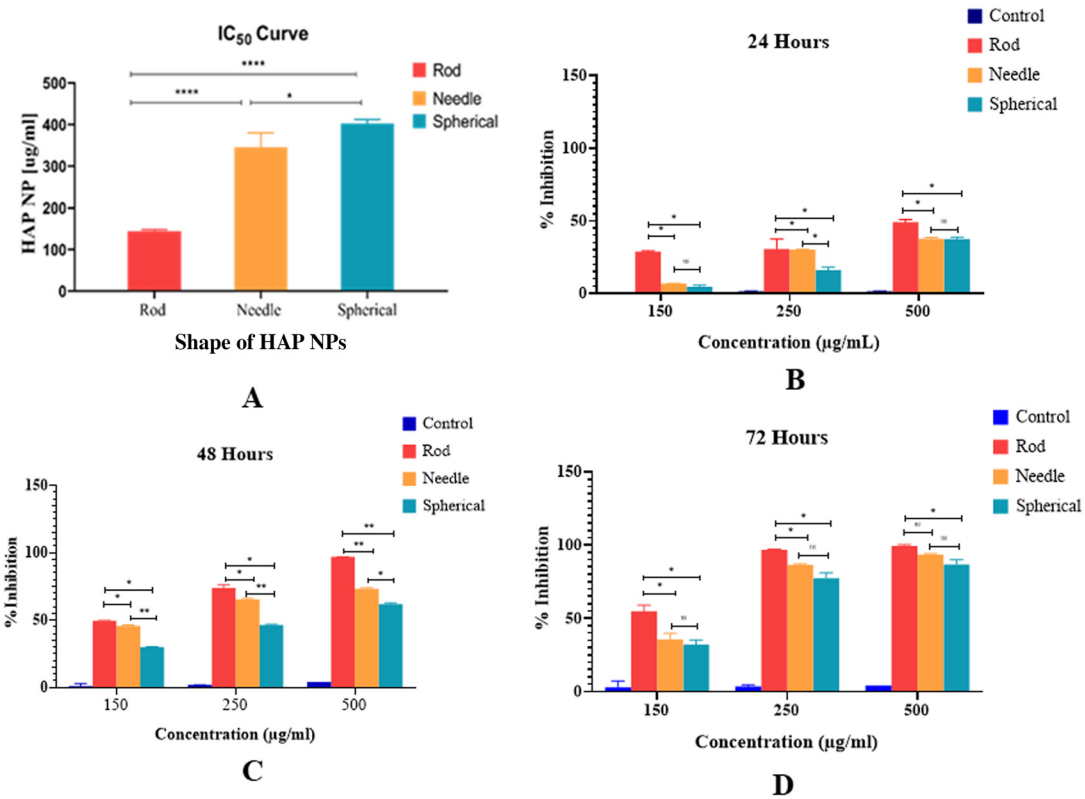

Fig. 3 MTT assay for HAP NPs of different shapes at different intervals: (A) IC_{50} graph, (B) 24 hours, (C) 48 hours, and (D) 72 hours of incubation with MG-63 cell lines at three different concentrations: 150, 250, and 500 µg ml^{-1} (n = 3, mean ± SE).

HAP NPs revealed good uptake in the MG63 osteosarcoma cell line, as shown in Fig. 2. The green fluorescent rod- and needle-shaped HAP NPs were detected primarily near the lysosomes (red) and nucleus (blue). This suggested their ability to escape the endosomal compartments and migrate deeper into the cytoplasm, attributed to their elongated shape facilitating interactions with the cytoskeleton and active transport along microtubules. In contrast, the spherical HAP NPs accumulated more at the cell periphery, possibly due to their entrapment in early endosomal compartments, restricting further intracellular movement.[43] Amini *et al.* further proposed that altering nanoparticle morphology could enhance drug delivery effectiveness and boost anticancer activity,[44] reiterating that shape-induced differences in intracellular trafficking could influence the anticancer efficacy.

Anticancer efficacy

The anticancer efficacy studies confirmed that HAP NP shape played an important role in anticancer efficacy.

MTT assay. The time-dependent cytotoxic effect of HAP NPs was observed (Fig. 3B–D). Overall, rod-shaped HAP NPs exhibited a significantly lower IC_{50} value compared to needle-shaped and spherical HAP NPs, suggesting enhanced anticancer efficacy (Fig. 3A). At high concentrations (500 μg mL^{-1}), maximum inhibition occurred at 48 hours, whereas at lower concentrations, peak inhibition was delayed and was observed at 72 hours. At concentrations of 250 and 500 μg mL^{-1} (Fig. 3D), the cytotoxicity of rod- and needle-shaped particles was comparable at 72 hours. Statistical analysis revealed significant differences in cytotoxicity between rod- and needle-shaped NPs ($p < 0.05$) and between rod- and spherical-shaped NPs ($p < 0.05$). However, the anticancer efficacy of needle-shaped and spherical NPs was comparable ($p > 0.05$). Across all concentrations, rod-shaped NPs exhibited the highest anticancer efficacy, followed by needle-shaped NPs, while spherical NPs showed the lowest efficacy. Our findings highlight the critical role of nanoparticle shape in influencing the efficacy and suggest that the differences may be ascribed to shape-mediated differences in intracellular trafficking and thereby the intracellular fate of the HAP NPs.

Clonogenic assay. The clonogenic assay, or colony formation assay, evaluates a cell's ability to propagate a colony from a

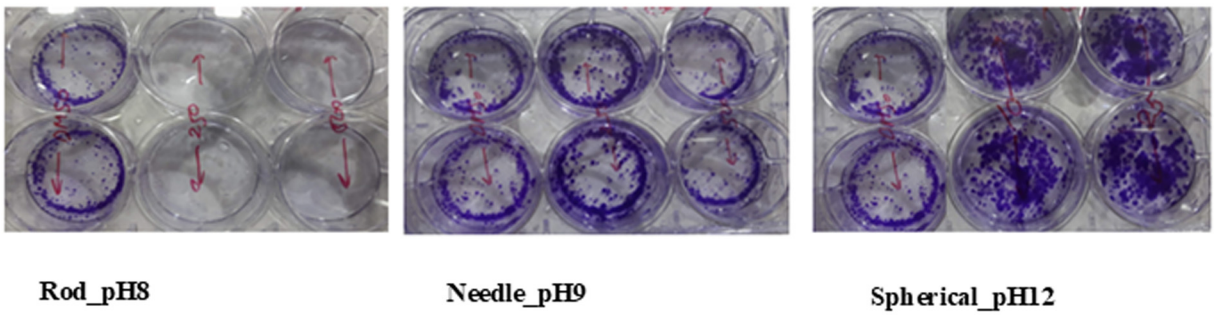

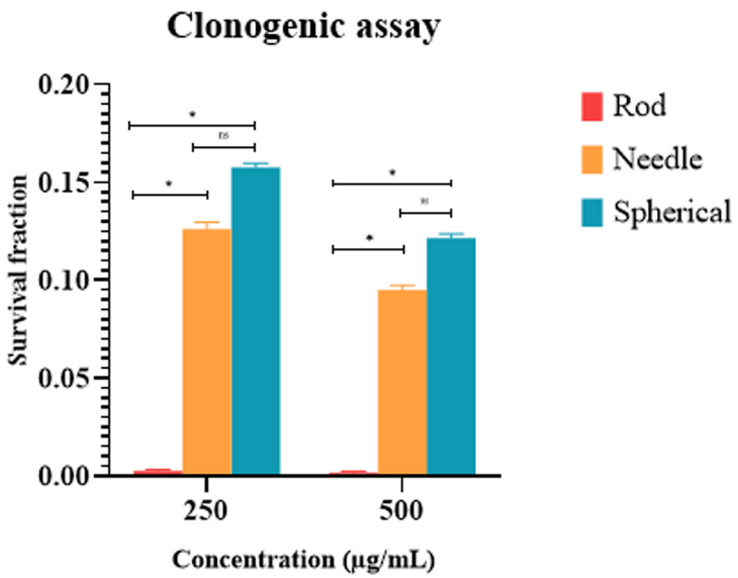

Fig. 4 Clonogenic assay for HAP NPs of different shapes after 14 days of incubation with MG-63 cell lines at two different concentrations: 250 and 500 μg ml^{-1} (n = 2). (A) Representative images of the dishes containing colonies. (B) The graph shows the survival fraction (n = 3, mean ± SE).

solitary cell *in vitro*, where a colony consists of fifty or more cells. The assay determines each cell's capacity for infinite division. The rod-shaped HAP NPs exhibited significantly higher inhibition of clonogenic survival, nearly completely suppressing colony formation, followed by the needle- and spherical-shaped HAP NPs in MG-63 osteosarcoma cells (Fig. 4A and B). Statistical analysis revealed significant differences in the survival fraction between rod- and needle-shaped NPs ($p < 0.05$) and between rod-shaped and spherical NPs ($p < 0.05$). However, no significant difference was observed between needle-shaped and spherical NPs ($p > 0.05$), corroborating the MTT assay results.

Cell scratch and transwell migration assay. The cell scratch and transwell migration assays were used to evaluate the efficacy of HAP NPs in inhibiting the invasive and metastatic potential of the MG-63 osteosarcoma cell line. Among the three, rod-shaped HAP NPs showed complete inhibition of the directional movement of MG-63 cells. In contrast, needle- and spherical-shaped HAP NP MG-63 cells showed some directional movement after 48 hours, which was comparable to the control (Fig. 5).

In the transwell migration assay, extensive migration was seen in the control. All the HAP NPs revealed lower migration in the order rod < needle ≪ spherical (Fig. 6). This suggests maximum efficacy with the rod-shaped NPs.

Hoechst/PI double staining assay. The compacted state of chromatin in apoptotic cells can be quickly and conveniently assessed using the double staining apoptosis assay. The

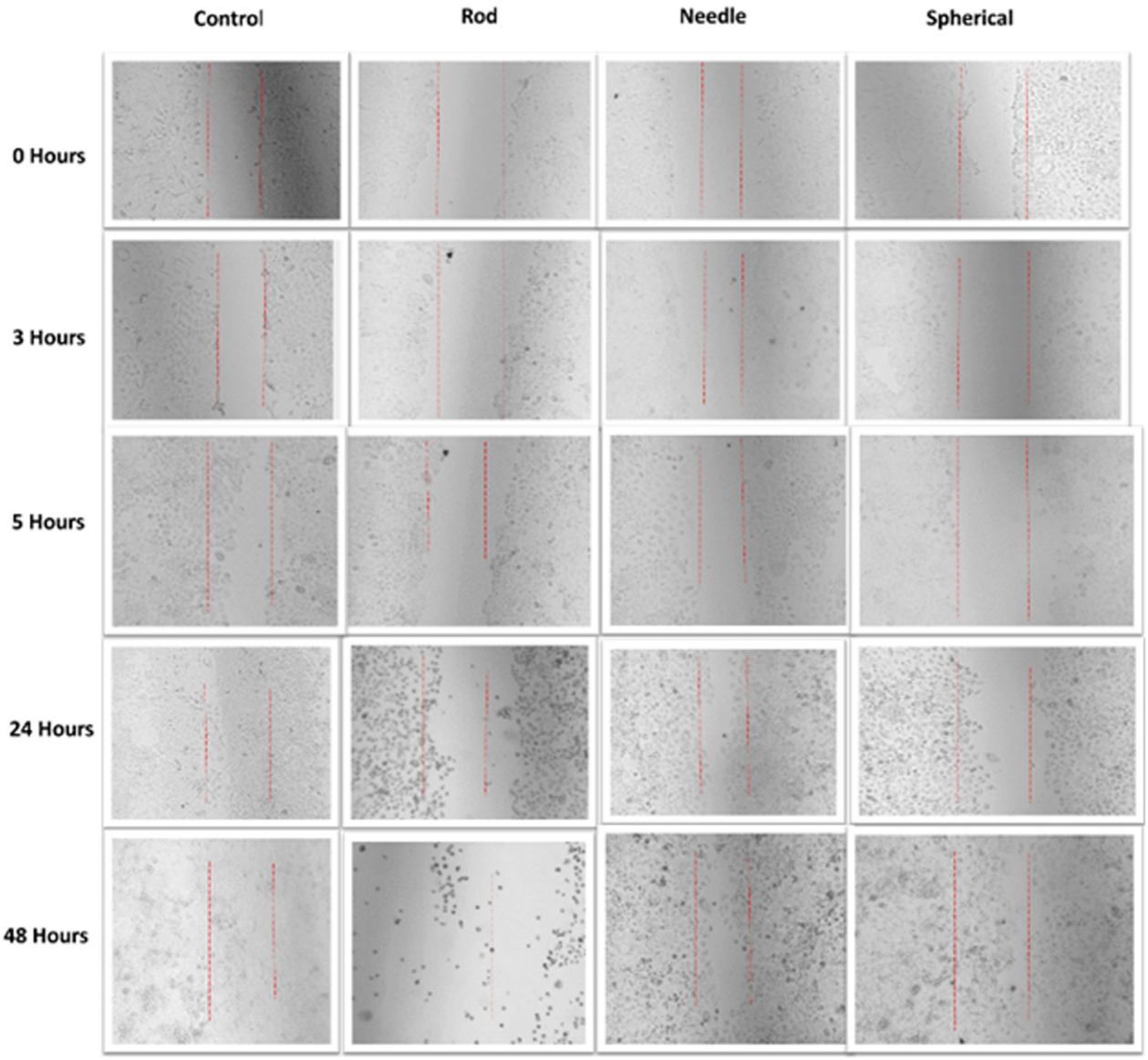

Fig. 5 Cell scratch assay: representative images indicate that at 100 μg ml^{-1}, rod-shaped HAP NPs show complete inhibition of the directional movement of MG-63 cells after 48 hours. At 100 μg ml^{-1}, needle- and spherical-shaped HAP NPs allowed MG-63 cells to show a slight directional movement after 48 hours compared to the control (n = 3, mean ± SE).

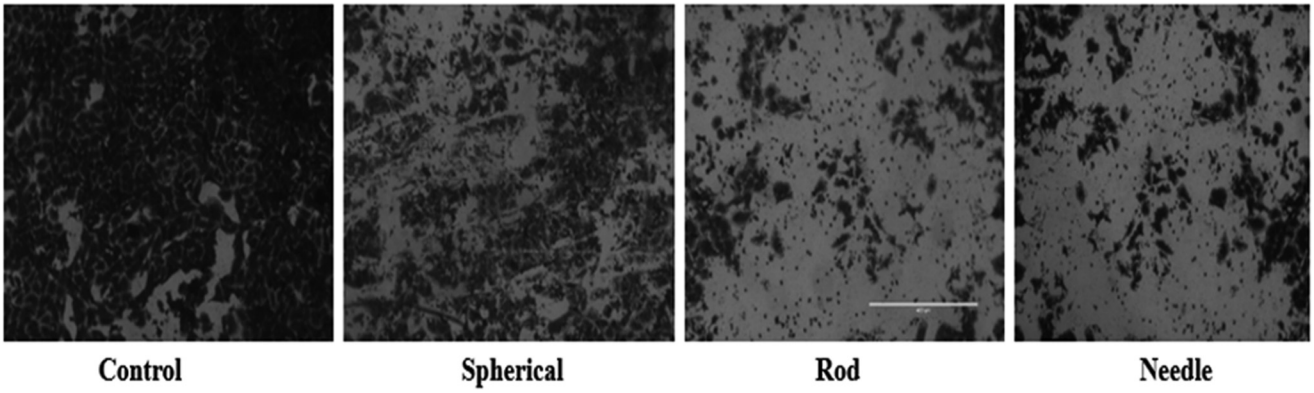

Fig. 6 Transwell migration assay: representative images indicate that at 100 μg ml^{-1}, rod-shaped HAP NPs are able to intervene in the migration of MG-63 cells towards the chemoattractant (n = 3, mean ± SE).

Hoechst dye can pass through cell membranes easily and can be used to stain the DNA of both living and dead cells and has been utilized to measure the total cell count. In contrast, the entry of PI is limited to cells with damaged plasma membranes, allowing it to mark deceased cells specifically. The MG-63 cells of the control group showed low-intensity blue fluorescence with Hoechst 33342 dye, and the cell boundaries appeared normal (Fig. S5†). There were no signs of nuclear breakdown or loss of integrity, and further there was no expression of apoptosis or necrosis. However, cells treated with rod-shaped, needle-shaped and spherical HAP NPs exhibited blue fluorescence of high intensity attributed to apoptosis, while the necrotic cells revealed red nuclear staining (PI). The rod-shaped HAP NP treated cells showed significant morphological changes and suppressed the growth of MG-63 osteosarcoma cells.

Conclusion

Our study demonstrates the anticancer efficacy of HAP NPs, while highlighting the role of HAP NP shape as an important parameter, which may be tailored to optimize the anticancer efficacy of HAP NPs.

Author contributions

Simmi Gupta: investigation, methodology, validation, and writing – original draft. Esha Attar: writing – review & editing. Vishvesh Joshi: data interpretation and writing – review & editing. Padma V. Devarajan: conceptualization, supervision, resources, funding acquisition and writing and editing the final draft.

Data availability

The data supporting this article have been included as part of the ESI.†

Conflicts of interest

The authors declare no conflicts of interest or personal relationships that might have biased their reported findings.

Acknowledgements

The financial support from GAT-B (formerly JNU CEEB), Department of Biotechnology, Government of India, to Simmi Gupta is gratefully acknowledged.

References

1 L. L. Hench and J. M. Polak, *Science*, 2002, **295**, 1014–1017.
2 V. S. Kattimani, S. Kondaka and K. P. Lingamaneni, *Bone Tissue Regener. Insights*, 2016, **7**, BTRI.S36138.
3 V. Saxena, I. Shukla and L. M. Pandey, in *Materials for biomedical engineering*, Elsevier, 2019, pp. 205–249.
4 Z. Bal, T. Kaito, F. Korkusuz and H. Yoshikawa, *Emergent Mater.*, 2020, **3**, 521–544.
5 A. Alivisatos, *Science*, 2000, **289**, 736–737.
6 R. Rial, M. González-Durruthy, Z. Liu and J. M. Ruso, *Molecules*, 2021, **26**, 3190.
7 V. Uskoković and D. P. Uskoković, *J. Biomed. Mater. Res., Part B*, 2011, **96**, 152–191.
8 K. Lin and J. Chang, in *Hydroxyapatite (HAp) for biomedical applications*, Elsevier, 2015, pp. 3–19.
9 H. Wu, Z. Li, J. Tang, X. Yang, Y. Zhou, B. Guo, L. Wang, X. Zhu, C. Tu and X. Zhang, *Int. J. Nanomed.*, 2019, 1177–1191.
10 S. Dey, M. Das and V. K. Balla, *Mater. Sci. Eng., C*, 2014, **39**, 336–339.
11 J. Jin, G. Zuo, G. Xiong, H. Luo, Q. Li, C. Ma, D. Li, F. Gu, Y. Ma and Y. Wan, *J. Mater. Sci.: Mater. Med.*, 2014, **25**, 1025–1031.
12 X. Chen, C. Deng, S. Tang and M. Zhang, *Biol. Pharm. Bull.*, 2007, **30**, 128–132.

13 Y. Yuan, C. Liu, J. Qian, J. Wang and Y. Zhang, *Biomaterials*, 2010, **31**, 730–740.
14 J. Hu, Z.-S. Liu, S.-L. Tang and Y.-M. He, *World J. Gastroenterol.*, 2007, **13**, 2798.
15 G. Guo, A. Tian, X. Lan, C. Fu, Z. Yan and C. Wang, *Exp. Ther. Med.*, 2019, **17**, 4080–4088.
16 W. Tang, Y. Yuan, C. Liu, Y. Wu, X. Lu and J. Qian, *Nanomedicine*, 2014, **9**, 397–412.
17 F. Qing, Z. Wang, Y. Hong, M. Liu, B. Guo, H. Luo and X. Zhang, *J. Mater. Sci.: Mater. Med.*, 2012, **23**, 2245–2251.
18 R. Wang, W. Liu, Q. Wang, G. Li, B. Wan, Y. Sun, X. Niu, D. Chen and W. Tian, *Biomater. Sci.*, 2020, **8**, 4426–4437.
19 M. d. C. De Lama-Odría, L. J. Del Valle and J. Puiggalí, *Int. J. Mol. Sci.*, 2022, **23**, 11352.
20 S. Kargozar, S. Mollazadeh, F. Kermani, T. J. Webster, S. Nazarnezhad, S. Hamzehlou and F. Baino, *J. Funct. Biomater.*, 2022, **13**, 100.
21 Q. Zhang, L. Qiang, Y. Liu, M. Fan, X. Si and P. Zheng, *Front. Bioeng. Biotechnol.*, 2023, **11**, 1167474.
22 S. R. Prasad, A. Jayakrishnan and T. S. Kumar, *J. Mater. Sci.: Mater. Med.*, 2020, **31**, 1–11.
23 T. Yu, Z. Cai, X. Chang, C. Xing, S. White, X. Guo and J. Jin, *Orthop. Surg.*, 2023, **15**, 2244–2259.
24 Y. Liu, A. Nadeem, S. Sebastian, M. A. Olsson, S. N. Wai, E. Styring, J. Engellau, H. Isaksson, M. Tägil and L. Lidgren, *Mater. Today Bio*, 2022, **14**, 100227.
25 K. P. Steckiewicz and I. Inkielewicz-Stepniak, *Nanomaterials*, 2020, **10**, 658.
26 S. Behzadi, V. Serpooshan, W. Tao, M. A. Hamaly, M. Y. Alkawareek, E. C. Dreaden, D. Brown, A. M. Alkilany, O. C. Farokhzad and M. Mahmoudi, *Chem. Soc. Rev.*, 2017, **46**, 4218–4244.
27 L. Chen, J. M. Mccrate, J. C. Lee and H. Li, *Nanotechnology*, 2011, **22**, 105708.
28 P. Foroozandeh and A. A. Aziz, *Nanoscale Res. Lett.*, 2018, **13**, 339.
29 L. Guerrini, R. A. Alvarez-Puebla and N. Pazos-Perez, *Materials*, 2018, **11**, 1154.
30 A. B. Jindal, *Int. J. Pharm.*, 2017, **532**, 450–465.
31 P. V. Devarajan, A. B. Jindal, R. R. Patil, F. Mulla, R. V. Gaikwad and A. Samad, *J. Pharm. Sci.*, 2010, **99**, 2576–2581.
32 G. Qian, L. Xiong and Q. Ye, *RSC Adv.*, 2023, **13**, 16512–16528.
33 C. Qi, S. Musetti, L.-H. Fu, Y.-J. Zhu and L. Huang, *Chem. Soc. Rev.*, 2019, **48**, 2698–2737.
34 Y. Han, S. Li, X. Cao, L. Yuan, Y. Wang, Y. Yin, T. Qiu, H. Dai and X. Wang, *Sci. Rep.*, 2014, **4**, 7134.
35 V. Varadarajan and S. V. Shankar, Comparative studies of hydroxyapatite (HAp) nanoparticles synthesized by using different green templates, In AIP Conference Proceedings, AIP Publishing, 2020, Vol. 2240.
36 S. Lara-Ochoa, W. Ortega-Lara and C. E. Guerrero-Beltrán, *Pharmaceutics*, 2021, **13**, 1642.
37 L. Tang, N. P. Gabrielson, F. M. Uckun, T. M. Fan and J. Cheng, *Mol. Pharm.*, 2013, **10**, 883–892.
38 K. Y. Win and S.-S. Feng, *Biomaterials*, 2005, **26**, 2713–2722.
39 V. T. Cong, K. Gaus, R. D. Tilley and J. J. Gooding, *Expert Opin. Drug Delivery*, 2018, **15**, 881–892.
40 D. J. Kotak and P. V. Devarajan, *Nanomedicine*, 2020, **24**, 102153.
41 H. Lv, J. Guo, S. Li and D. Jiang, *Exp. Ther. Med.*, 2014, **8**, 1575–1580.
42 Y. Lu, W. Dong, J. Ding, W. Wang and A. Wang, in *Nanomaterials from clay minerals*, Elsevier, 2019, pp. 485–536.
43 C. Zhu, X. Zhou, Z. Liu, H. Chen, H. Wu, X. Yang, X. Zhu, J. Ma and H. Dong, *Front. Mol. Biosci.*, 2021, **8**, 627015.
44 M. A. Amini, T. Ahmed, F.-C. F. Liu, A. Z. Abbasi, C. D. Soeandy, R. X. Zhang, P. Prashad, C. L. Cummins, A. M. Rauth and J. T. Henderson, *Expert Opin. Drug Delivery*, 2021, **18**, 991–1004.